DOI: https://doi.org/10.21009/JRSKT.121.05

Rice Husk Silica-Based magMCM-41 Composites: Synthesis, Characterization, and Pb(II) Adsorption Performance

Nita Trisnawati[1], Eti Rohaeti[1*a)], Deden Saprudin[1*b)], Sarah Yasir[2*c)]

[1]*Department of Chemistry, Faculty of Mathematics and Science, Bogor Agricultural University, Jalan Tanjung Kampus IPB, Dramaga, Bogor*
[2]*Energy Research Cluster, Zero Carbon Manufacturing, Business and Energy Research Centre, University of Derby, Kedleston Road, Derby, DE22 1GB, United Kingdom*

*Email: a)etirohaeti@apps.ipb.ac.id (E.R.); b)dsp@apps.ipb.ac.id (D.S.); c)s.yasir@derby.ac.uk (S.Y.)

Received: 26 April 2026
Revised: 15 May 2026
Accepted: 28 May 2026
Online: 24 June 2026
Published: 30 June 2026

Jurnal Riset Sains dan Kimia Terapan
p-ISSN: 2302 - 8467
e-ISSN: 2303 – 0720

Abstract

Lead (Pb) contamination in water poses serious environmental and health risks, necessitating the development of effective and sustainable adsorbents for its removal. This study aimed to synthesize and characterize magMCM-41 composites derived from rice husk silica, and evaluate their performance for Pb(II) ion removal in aqueous solutions. The magMCM-41 was prepared by integrating magnetite (Fe_3O_4) nanoparticles into a mesoporous silica framework via co-preparation and sol-gel methods using cetyltrimethylammonium bromide (CTAB) as a template. Characterization by XRD, FTIR, BET, and PSA confirmed successful composite formation, revealing a high specific surface area of 476.744 m^2/g, a mesoporous framework (pore diameter 3.83 nm), and an average particle size of 362.7 nm. Adsorption conditions were optimized using Response Surface Methodology (RSM); pH positively influenced capacity, whereas adsorbent dosage had a negative effect. The maximum adsorption capacity was 115.77 mg/g at pH 5 with 0.05 g of adsorbent. The Dubinin-Radushkevich model best described the adsorption equilibrium (R^2=0.935), indicating physisorption on a heterogeneous surface. Thermodynamic analysis confirmed a spontaneous and exothermic process. These results demonstrate that rice husk-derived magMCM-41 is a sustainable and magnetically separable adsorbent with high potential for Pb(II) remediation.

Keywords: adsorption, magMCM-41, magnetic adsorbent, Pb(II), rice husk silica

Introduction

Heavy metal pollution in aquatic environments is a serious problem that directly impacts human health and ecosystem sustainability. One of the heavy metals of primary concern is lead (Pb), due to its toxicity, persistence, and ability to accumulate in biological tissues. Lead contamination in drinking water is a major global concern, as the World Health Organization (WHO) has established a guideline value of 0.01 mg/L (10 µg/L) as the maximum permissible limit for Pb in drinking water. Long-term exposure to Pb even below this threshold can cause disorders of the nervous system, kidneys, and cognitive development, particularly in children, even at relatively low concentrations. Therefore, the removal of Pb(II) from aqueous systems is essential to protect both environmental and human health.

Various treatment methods have been developed for Pb(II) removal, including chemical precipitation, ion exchange, membrane filtration (Lu et al., 2025), and adsorption (Wu et al., 2019). Among these methods, adsorption is widely recognized as one of the most effective techniques due to its simplicity, high efficiency, and economic feasibility (He et al., 2019; Wu et al., 2019). The performance of adsorption processes is strongly influenced by the characteristics of the adsorbent, particularly its surface area, pore structure, and surface functional groups.

Recently, biomass-derived materials have gained significant attention as low-cost and sustainable adsorbents due to their renewable nature and rich functional group content. Various agricultural and plant-based wastes have been explored as biosorbent precursors, including bamboo root cellulose and tea waste products. For instance, Wulandari et al. (2023) demonstrated that bamboo root cellulose activated with dilute nitric acid achieved a maximum Fe(II) adsorption capacity of 3.56 mg/g. While Wulandari et al. (2022) reported that green tea waste achieved a maximum adsorption capacity of 47 mg/g for Rhodamine-B removal, confirming tea waste as a feasible low-cost biosorbent. However, these cellulose-based biomass adsorbents generally suffer from relatively low adsorption capacity for heavy metal ions such as Pb(II), limited surface area, and poor structural ordering, which restrict their broader applicability for heavy metal remediation. To overcome these limitations, attention has shifted toward biomass sources with naturally high silica content as precursors for more structured and high-performance adsorbents. Various agricultural by-products have been explored as silica precursors, including sugarcane bagasse (~1-3% SiO_2), wheat straw (~3-7%), corn cob (~1-2%), and bamboo (~2-5%). However, these sources generally suffer from low silica content, high impurity levels, and the need for extensive purification, which limits their practicality for producing high-purity mesoporous silica. In contrast, rice husk stands out as the most promising silica precursor, containing approximately 15-20% SiO_2 (Soltani et al., 2015), making it the most abundant and economically viable precursor for high-purity silica-based adsorbent globally. Prior research has demonstrated various modifications of rice husk-derived silica to improve its heavy metal adsorption performance: early studies focused on amino-functionalization using silane coupling agents such as 3-aminopropyltrimethoxysilane (APTMS) (Nurhajawarsi et al., 2018; Rohaeti et al., 2020), followed by amino acid grafting with L-histidine and L-lysine to introduce chelating functional groups capable of coordinating with Pb(II) ions. While these modifications improved adsorption capacity, the resulting materials were limited to simple silica supports without structured mesoporosity. More recently, silica from rice husk has been used to synthesize MCM-41-type mesoporous materials, which offer a highly ordered hexagonal pore structure (pore diameter ~2-4 nm) and dramatically higher surface area (300-900 m^2/g) compared to conventional silica (Chun et al., 2020). The combination of structured mesoporosity with surface functionalization has emerged as the most effective strategy for Pb(II) adsorption, as it simultaneously provides more active sites, improved accessibility, and stronger coordination.

Several studies have demonstrated the potential of rice husk silica-based materials for Pb(II) adsorption. For example, L-histidine-modified silica showed an adsorption capacity of 62.5 mg/g (Nurhajawarsi et al., 2018), while L-lysine-modified silica reached 71.88 mg/g (Rohaeti et al., 2020). Furthermore, amine-functionalized magMCM-41 synthesized from rice husk silica exhibited significantly higher adsorption capacity up to 540.64 mg/g (Kamari et al., 2019), highlighting the importance of structural modification in enhancing adsorption performance. It is important to note that the work by Kamari et al. (2019) employed NH_2-functionalized magMCM-41 synthesized through a one-pot co-condensation approach and targeted a different metal ion (Pb(II) via amine chelation), achieving its exceptionally high capacity partly through chemical adsorption. In contrast, the present study synthesizes non-functionalized magMCM-41 without additional amine grafting, using a distinctly different synthesis strategy in which Fe_3O_4 nanoparticles are pre-synthesized separately and subsequently incorporated into the silica framework via a modified sol-gel method. This approach allows better control over the Fe_3O_4 nanoparticle size and distribution within the mesoporous structure, potentially improving the composite's magnetic properties and structural integrity. Furthermore, this work employs RSM-FCCCD for optimization and examines the adsorption mechanism through multiple isotherm models and thermodynamic analysis, which provides new insight into the physisorption-dominated removal of Pb(II) on a heterogeneous surface – a mechanistic aspect not thoroughly addressed by Kamari et al., (2019).

Despite these advantages, conventional mesoporous silica materials face practical limitations in separation from aqueous solutions due to their fine particle size. To address this issue, the incorporation of magnetic materials into the silica framework has been widely explored. Among the various magnetic materials available, magnetite (Fe_3O_4) in the silica framework has been widely explored (Ghiasi & Malekpour, 2020; Kamari & Ghorbani, 2017; Sulejmanović et al., 2019). Magnetic adsorbents enable rapid and efficient separation using an external magnetic field, improving the practicality of the adsorption process (Kobylinska et al., 2020). Among the various magnetic materials available, Fe_3O_4 is the preferred choice due to its well-established biocompatibility, chemical stability under a wide pH range, strong superparamagnetic behavior enabling rapid magnetic separation, and ease of synthesis via co-precipitation. Other magnetic materials, such as cobalt ferrite ($CoFe_2O_4$) and nickel ferrite ($NiFe_2O_4$) have also been explored; however, their potential cytotoxicity and more complex synthesis limit their practical applicability. The study by Kobylinska et al. (2020), while also employing magnetite-based materials, focused on EDTA-functionalized Fe_3O_4 nanoparticles for multi-element heavy metal extraction using ICP-OES detection, primarily targeting trace-level analysis rather than adsorptive remediation from bulk solutions. In contrast, the present study uses Fe_3O_4 as a structural component embedded within the MCM-41 mesoporous framework, creating a composite adsorbent (magMCM-41) designed for high-capacity Pb(II) removal. The use of nanoscale Fe_3O_4 (rather than bulk magnetite) is essential in this work: nanoparticles provide significantly higher surface area, stronger magnetic response per unit mass, and better dispersibility within the silica matrix, ensuring uniform composite formation and effective separation after adsorption.

Based on these considerations, this study focuses on the synthesis of magMCM-41 composites derived from rice husk silica and Fe_3O_4 nanoparticles. The prepared material was characterized using various techniques and evaluated for its adsorption performance toward Pb(II) ions. The novelty of this work lies in three key aspects: (1) the use of rice husk as a low-cost, sustainable silica source to synthesize the MCM-41 mesoporous framework; (2) the pre-synthesis and separate incorporation of Fe_3O_4 nanoparticles into the silica matrix via a modified sol-gel method, providing better control of nanoparticle distribution than co-condensation approaches; and (3) the comprehensive mechanistic study combining RSM optimization, multiple isotherm modeling, and thermodynamic analysis to elucidate the physisorption-dominated Pb(II) removal mechanism on the heterogeneous magMCM-41 composite. Collectively, this work aims to develop a sustainable, high-capacity, and magnetically recoverable adsorbent derived from agricultural waste and to provide a deeper understanding of the underlying adsorption mechanism, filling gaps not addressed in existing literature.

Method

Materials and Instrumentation.

The materials used in this research include: rice husk charcoal, hydrochloric acid (HCl, 37%, Merck), sodium hydroxide (NaOH), aquabides, ammonium hydroxide (NH_4OH, 25%, Merck), iron salts ($FeCl_3.6H_2O$ and $FeSO_4.7H_2O$), cetyltrimethylammonium bromide (CTAB) as a template, lead nitrate ($Pb(NO_3)_2$, nitric acid (HNO_3, 65%, Merck), and filter paper. The instrumentation used includes: analytical balance, furnace, oven, and a hydrothermal reactor. Solution preparation and homogenization utilized a pH meter, shaker, sonicator, and a hot plate equipped with a magnetic stirrer, along with standard glassware and an external magnet for magnetic recovery. Characterization of the synthesized materials was conducted using Fourier-Transform Infrared Spectroscopy (FTIR, Shimadzu IR Prestige-21), X-Ray Diffraction (XRD, Bruker D8 Advance), Particle Size Analysis (PSA, Horiba-Sz 100z), and Brunauer-Emmett-Teller analysis (BET, Quantachrome Quadrasorb-Evo Surface Area and Pore Size Analyzer). The concentration of lead ions during adsorption was determined using Atomic Absorption Spectroscopy (AAS, Shimadzu AA-7800).

Synthesis of Silica from Rice Husk.

Silica was extracted from rice husk ash following a previously reported method with slight modifications (Hasri et al., 2023; Kamari & Ghorbani, 2021). The rice husk charcoal was first treated with 1 M HCl at 100 ˚C to remove impurities, washed to neutral pH, and calcined at 600 ˚C for 4 h. The obtained ash was dissolved in 2.5 N NaOH at 80-100 ˚C to produce a sodium silicate solution. The solution was then subjected to hydrothermal treatment at 120 ˚C for 6 h. Silica gel was formed by adjusting the pH to 7 using 1 M HCl, followed by aging, washing, and drying at 105 ˚C.

Synthesis of Fe_3O_4 Nanoparticles.

Magnetite nanoparticles were synthesized using the co-precipitation method based on (Rahimah et al., 2019) with minor adjustments. Fe^{3+} and Fe^{2+} salts (molar rasio 2:1) were dissolved in distilled water and mixed under stirring. NH_4OH (25%) was added dropwise until pH 10 to form a black precipitate of Fe_3O_4. The precipitate was washed and dried at 60 ˚C. This method was selected due to its simplicity and ability to produce nanoscale magnetite with good magnetic properties.

Synthesis of magMCM-41 Composite.

The magMCM-41 composite was synthesized using a modified sol-gel method adapted from (Kamari & Ghorbani, 2021). Unlike the original method, Fe_3O_4 nanoparticles were synthesized separately and then introduced into the silica framework. CTAB was used as a structure-directing agent in an alkaline medium (NH_4OH). The Fe_3O_4 suspension was added gradually into the CTAB solution under continuous stirring, followed by the addition of silica precursor derived from rice husk. The mixture was stirred for 6 h, aged at 100 ˚C for 72 h, and then filtered, washed, and dried. Finally, calcination at 550 ˚C for 5 h was carried out to remove the surfactant template and obtain the mesoporous structure.

Characterization Techniques.

Functional groups of the synthesized materials (silica, Fe_3O_4, and magMCM-41) were analyzed using Fourier-Transform Infrared Spectroscopy (FTIR, Shimadzu IR Prestige-21, Japan). Samples were prepared by mixing with KBr powder and pressed into pellets. Spectra were recorded in transmittance mode over a wavenumber range of 400-4000 cm^{-1} with a resolution of 4 cm^{-1} and a minimum of 16 scans per measurement. Identification of functional groups was performed by comparing the observed absorption bands with standard reference spectra.

The crystal structure, phase composition, and crystallinity of the synthesized materials were analyzed using X-Ray Diffraction (XRD, Bruker D8 Advance, Germany) with monochromatic CuKα radiation (λ=1.54056 Å) operating at 40 kV and 40 mA. Diffraction patterns were recorded over a 2θ range of 10˚-80˚ with a step size of 0.02˚ and a scan rate of 2˚ min^{-1}. Phase identification was performed by comparing the diffraction peaks with the Joint Committee on Powder Diffraction Standards (JCPDS) reference card No. 19-0629 for magnetite (Fe_3O_4). The average crystallite size was calculated using the Scherrer equation:

$$D = \frac{K\lambda}{\beta \cos \theta} \tag{1}$$

Where D is the average crystallite size (nm), K is the Scherrer constant (0.89), λ is the X-Ray wavelength (nm), β is the full width at half maximum (FWHM) in radians, and θ is the Bragg diffraction angle.

The specific surface area, pore volume, and pore diameter of the synthesized materials were determined using the Brunauer-Emmett-Teller (BET) method with a Quantachrome Quadrasorb-Evo Surface Area and Pore Size Analyzer (USA). Prior to measurement, samples were degassed at 100 ˚C for 3 hours under vacuum to remove adsorbed moisture and impurities. Nitrogen adsorption-desorption isotherms were recorded at -196 ˚C (77 K). The specific surface area was calculated using the multi-point BET equation, while the total pore volume was determined from the amount of N_2 adsorbed at a relative pressure (P/P_0) of 0.99. The average pore diameter was calculated using the Barrett-Joyner-Halenda (BJH) method applied to the desorption branch of the isotherm. The pore structure type was classified according to IUPAC recommendations based on the shape of the isotherm and the hysteresis loop.

Particle size distribution and the hydrodynamic diameter of the synthesized materials were measured using Particle Size Analysis (PSA, Horiba SZ-100z, Japan) based on the dynamic light scattering (DLS) principle. Samples were dispersed in aqueous solution and sonicated for 10 minutes prior to measurement to ensure adequate dispersion. Data are reported as mean diameter, mode, standard deviation (SD), Z-average, and polydispersity index (PI). The PI value indicated the breadth of the particle size distribution, where values below 0.3 indicate a relatively monodisperse system, while values above 0.5 indicate a broad or polydisperse distribution.

Adsorption Experiments.

Adsorption experiments were designed using Response Surface Methodology (RSM) with a face-centered central composite design (FCCCD). The effects of pH (3-5), contact time (50-120 min), and adsorbent dosage (0.05-0.15 g) were evaluated.

The adsorption capacity was calculated as:

$$q_e = \frac{(C_0 - C_e)V}{m} \tag{2}$$

Where q_e is the adsorption capacity (mg/g). C_0 and C_e are the initial and equilibrium concentration (mg/L), V is the solution volume (L), and m is the adsorbent mass (g).

The adsorption efficiency was calculated as:

$$\%R = \frac{(C_0 - C_e)}{C_0} \times 100 \tag{3}$$

Adsorption Isotherm Modelling.

The adsorption equilibrium data were analyzed using Langmuir, Freundlich, Temkin, and Dubinin-Radushkevich isotherm models.

The Langmuir equation is expressed as:

$$q_e = \frac{q_{max} K_L C_e}{1 + K_L C_e} \tag{4}$$

The Freundlich model is given by:

$$q_e = K_F C_e^{1/n} \tag{5}$$

The Temkin equation is expressed as:

$$q_e = B \ln(K_T C_e) \tag{6}$$

The Dubinin-Radushkevich equation is given by:

$$q_e = q_m exp(-\beta \varepsilon^2) \tag{7}$$

Where ε is calculated as:

$$\varepsilon = RT \ln\left(1 + \frac{1}{C_e}\right) \tag{8}$$

Result and Discussion

The Result of Structural and Functional Characterization.

The FTIR spectra of silica, Fe_3O_4, and magMCM-41 are presented in **Figure 1**, while the corresponding band assignments are summarized in **Table 1**. A broad absorption band around 3454 cm^{-1} is attributed to O-H stretching vibrations from silanol groups (≡Si-OH) and adsorbed water. The band at approximately 1630 cm^{-1} corresponds to O-H bending vibrations of adsorbed water molecules. These bands are characteristic of silica-based materials and are consistently reported in the literature. Kamari & Ghorbani (2021) similarly observed O-H stretching at ~3440 cm^{-1} and bending at ~1630 cm^{-1} in rice husk-derived silica, confirming the presence of surface silanol groups. The characteristic silica framework is confirmed by strong bands at 1086 cm^{-1} (asymmetric Si-O-Si stretching) and 801 cm^{-1} (symmetric stretching), which are the fingerprint bands of amorphous silica networks. The assignments are in good agreement with previous studies on MCM-41-type mesoporous silica, where asymmetric Si-O-Si stretching typically appears in the range of 1050-1100 cm^{-1} and symmetric stretching at 790-810 cm^{-1} (Raji et al., 2015; Stocki et al., 2024).

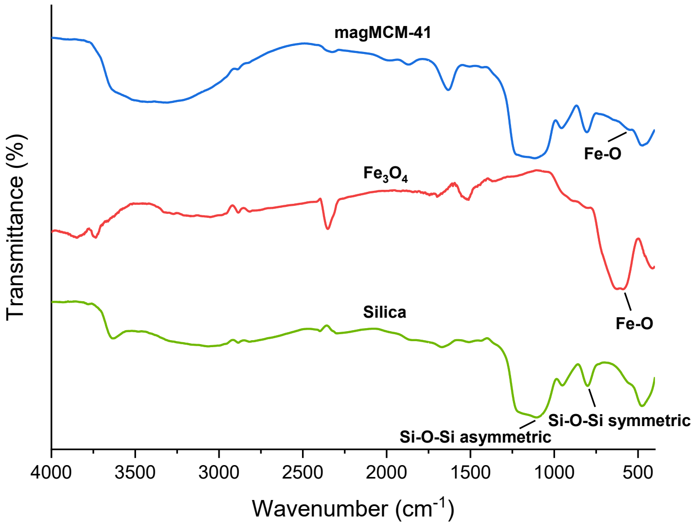

Figure 1. FTIR spectra of magMCM-41, Fe_3O_4, and silica

Importantly, the appearance of a band at ~553 cm^{-1} in both Fe_3O_4 and magMCM-41 spectra, corresponding to Fe-O stretching vibrations of magnetite, confirms the successful incorporation of magnetite into the silica framework. This band is characteristic of the Fe-O bond in the spinel structure of magnetite and has been consistently reported in the literature at 550-600 cm^{-1} for Fe_3O_4-containing composites (Ghiasi & Malekpour, 2020; Kobylinska et al., 2020). The simultaneous presence of Si-O-Si bands and the Fe-O band in the magMCM-41 spectrum demonstrates that the mesoporous silica structure was retained after incorporation of Fe_3O_4, and that the composite material possesses both the silanol functional groups necessary for Pb(II) coordination and the magnetic phase required for separation. These results are consistent with findings reported by Kamari et al. (2019) for amine-functionalized magMCM-41 synthesized from rice husk silica, where the Fe-O band at ~568 cm^{-1} confirmed magnetite integration without disruption of the silica framework.

Table 1. FTIR band assignments of silica, Fe_3O_4, and magMCM-41

Wavenumber (cm^{-1})	Assignment	Functional Group/Vibration	Sample
~3454	O-H stretching	Silanol (≡Si-OH)/adsorbed H_2O	Silica, Fe_3O_4, magMCM-41
~1630	O-H bending	Adsorbed H_2O	Silica, Fe_3O_4, magMCM-41
~1086	Asymmetric stretching	Si-O-Si	Silica, magMCM-41
~801	Symmetric stretching	Si-O-Si	Silica, magMCM-41
~553	Stretching vibration	Fe-O	Fe_3O_4, magMCM-41

The Result of Textural Properties (BET Analysis).

The nitrogen adsorption-desorption isotherms are shown in **Figure 2**. The magMCM-41 exhibits a typical type IV isotherm with a hysteresis loop, indicating a well-defined mesoporous structure with cylindrical pores according to IUPAC classification (Gabriel et al., 2023). This isotherm type is characteristic of ordered mesoporous silica materials such as MCM-41 and has been widely reported for silica-based composites (Raji et al., 2015; Stocki et al., 2024).

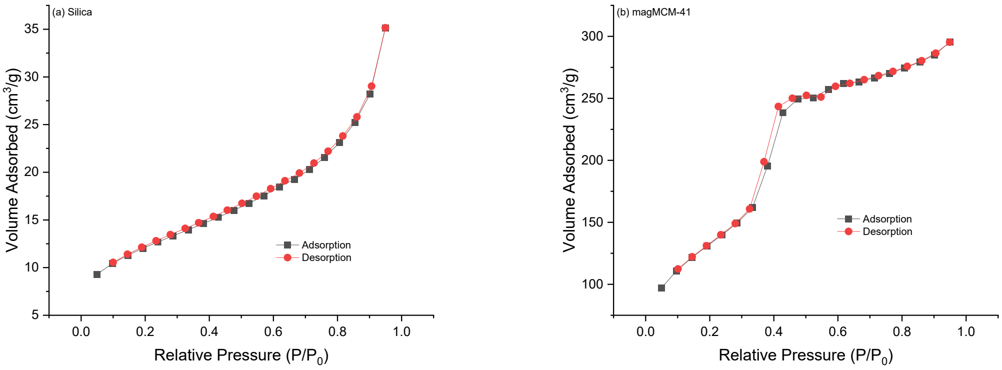

Figure 2. Adsorption-desorption isotherms of N_2 on silica (a) and magMCM-41 (b)

The BET results reveal a significant increase in specific surface area from 42.143 m^2/g (silica) to 476.744 m^2/g (magMCM-41), confirming that template-directed sol-gel synthesis using CTAB successfully generated an ordered mesoporous structure. This enhancement is comparable to values reported in the literature for magMCM-41 materials. Kamari & Ghorbani (2017) reported a BET surface area of ~695.7 m^2/g for magMCM-41 synthesized from rice husk silica. The slightly lower surface area observed in the present study (476.744 m^2/g) may be attributed to the pre-formed Fe_3O_4 nanoparticles partially occupying the pore channels, which is an expected consequence of the separate nanoparticle incorporation strategy employed here. Similarly, the total pore volume increases substantially from 0.05437 cm^3/g (silica) to 0.4569 cm^3/g (magMCM-41), indicating significantly improved pore accessibility, which is essential for efficient mass transfer of Pb(II) ions to the adsorbent's active sites.

The average pore diameter decreases from 5.16 nm (silica) to 3.83 nm (magMCM-41), yet remains well within the mesoporous range of 2-50 nm as defined by IUPAC (Jacobson et al., 2022). The pore diameter of 3.83 nm is consistent with the typical pore size range for MCM-41 materials (2-4 nm) and is in good agreement with values reported by Chun et al. (2020) for MCM-41 synthesized from rice husk silica (3-60 nm depending on surfactant conditions). The smaller and more uniform pore diameter of magMCM-41 compared to raw silica is a direct result of the CTAB template-directed pore formation, and contributes to better adsorption performance through increased surface area and a higher density of active sites per unit mass (Stocki et al., 2024).

The Result of Crystal Structure Analysis (XRD)

The XRD patterns of silica, Fe_3O_4, and magMCM-41 are shown in **Figure 3**. The diffraction peaks of Fe_3O_4 appear at $2\theta \approx 30\text{-}63^\circ$, corresponding to the crystal planes (220), (311), (400), (511), and (440), which match well with the standard JCPDS card No. 19-0629 for magnetite. The most intense peak at the (311) plane confirms the formation of crystalline, phase-pure magnetite. These characteristic diffraction peaks are in full agreement with Rahimah et al. (2019), who reported identical Fe_3O_4 peak positions at $2\theta \approx 30.28^\circ$, 35.67°, 43.36°, 57.36°, and 62.99° for magnetite synthesized by the co-precipitation method, confirming the spinel cubic structure.

In contrast, silica exhibits a broad peak at $2\theta \approx 20\text{-}25^\circ$, indicating its predominantly amorphous nature, which is typical of silica extracted from rice husk ash (Hasri et al., 2023; Kamari & Ghorbani, 2021). The presence of a minor sharp peak at 31.74° suggests a trace crystalline phase, likely associated with residual inorganic impurities from rice husk ash that were not fully removed during acid leaching. For magMCM-41, the characteristic peaks of Fe_3O_4 are preserved, confirming that the magnetic phase remains intact after the sol-gel synthesis and calcination at 550 °C. However, a significant decrease in peak intensity compared to pure Fe_3O_4 is observed, indicating that the magnetite nanoparticles are well dispersed and encapsulated within the amorphous silica matrix, as also reported by Kamari et al. (2019) for rice husk-derived magMCM-41.

The average crystallite size, calculated using the Scherrer equation, decreased from 22.32 nm (Fe_3O_4) to 18.59 nm (magMCM-41), as shown in **Table 2**. This reduction indicates that the mesoporous silica matrix effectively restricts crystal growth of the magnetite phase during the high-temperature calcination step. A similar trend was reported by Kamari & Ghorbani (2017), who observed a decrease in Fe_3O_4 crystallite size upon incorporation into the MCM-41 framework, which was attributed to spatial confinement within the silica pore walls. The reduction in crystallite size is beneficial for adsorption performance, as smaller crystallite size generally results in higher surface energy and more accessible active sites.

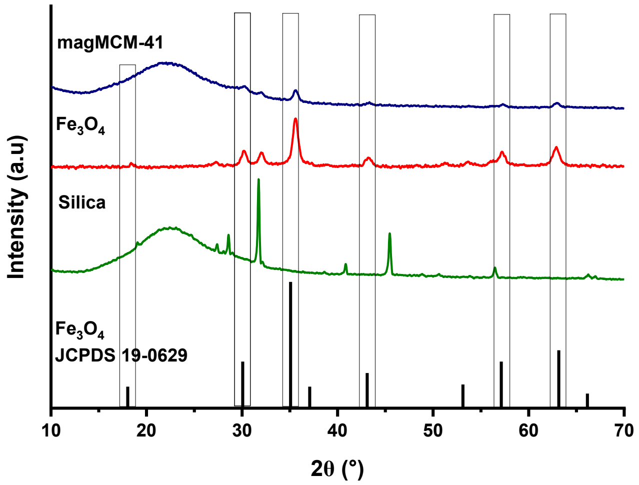

Figure 3. XRD diffraction patterns of silica, Fe_3O_4, and magMCM-41, as well as the JCPDS standard 19-0629

Table 2. Crystallographic parameters of adsorbents based on XRD analysis

Sample	*2θ* (°)	FWHM (β)	d-spacing (Å)	Average crystallite size (nm)
Silica	45.47	0.15	2.82	55.22
Magnetite	35.67	0.37	2.52	22.32
magMCM-41	35.57	0.45	2.52	18.59

The Result of Particle Size Distribution (PSA).

The particle size distribution data are summarized in **Table 3**. The mean particle size of silica, Fe_3O_4, and magMCM-41 are 386.4 nm, 355.3 nm, and 362.7 nm, respectively, as measured by dynamic light scattering (DLS). The intermediate particle size of magMCM-41 (362.7 nm) between those of silica (386.4 nm) and Fe_3O_4 (355.3 nm) is consistent with the formation of a composite material in which magnetite nanoparticles are embedded or coated within the silica matrix, resulting in a size that reflects the combined contribution of both components. This observation is supported by the Z-average values of 290.0 nm (silica), 264,5 nm (Fe_3O_4), and 286.3 nm (magMCM-41), which show a similar intermediate trend for the composite.

Table 3. Comparison of particle sizes based on PSA results

Sample	Mean (nm)	Mode (nm)	SD (nm)	Z-average (nm)	PI
Silica	386.4	334.8	150.5	290.0	0.753
Magnetit	355.3	296.6	148.0	264.5	0.647
magMCM-41	362.7	333.9	124.6	286.3	0.687

The polydispersity index (PI) values of 0.753 (silica), 0.647 (Fe_3O_4), and 0.687 (magMCM-41) indicate that all samples exhibit a broad, polydisperse size distribution, which is commonly observed for nanoparticle systems in aqueous suspension due to particle aggregation driven by surface energy and van der Waals forces (Leong et al., 2018). The PI value of magMCM-41 (0.687) is lower than that of raw silica (0.753), suggesting that the CTAB surfactant used during synthesis played an important role in controlling particle growth and reducing agglomeration through steric and electrostatic stabilization during the sol-gel process. Despite the broad distribution, the unimodal character of the size distribution curves indicates that the particles are still dominated by a single size particle population, with no evidence of multimodal aggregation states. It is important to note that DLS measures the hydrodynamic diameter, which is inherently larger than the crystallite size determined by

XRD (18.59 nm for magMCM-41), as DLS includes the solvation shell and any particle aggregates present in solution (Leong et al., 2018).

Optimization of Pb(II) Adsorption Conditions.

The optimization of Pb(II) adsorption conditions was conducted to achieve the maximum removal performance using the magMCM-41 composite. The variable optimized included solution pH, contact time, and adsorbent dosage, as these three factors significantly influence the interaction between Pb(II) ions and the active sites on the material surface. The optimum conditions were determined using RSM with FCCCD, allowing for a statistical evaluation of the individual effects and the interactions between variables.

The analysis result indicates that the solution pH has a positive influence on the adsorption of Pb(II) by the magMCM-41 composite. An increase in pH from acidic toward neutral conditions tends to enhance the adsorption capacity. At higher pH levels, the competition between H^+ ions and Pb^{2+} ions for the adsorbent's surface site decreases. It has been reported that the adsorption capacity reaches an optimal equilibrium state at approximately pH 4 (Xu et al., 2025). When the solution pH is below 3, both the capacity and rate of Pb(II) uptake are relatively low due to the high concentration of H^+ ions competing for active sites. Furthermore, an excess of H^+ ions can lead to the protonation of functional groups (such as silanol or iron-hydroxyl groups), resulting in a more positive surface charge that electrostatically repels Pb^{2+} cations. As the pH increases to the 4-5 range, the H^+ concentration diminishes, releasing negatively charged active sites ($Si\text{-}O^-$ or $Fe\text{-}O^-$) that can interact strongly with Pb^{2+} ions, thereby significantly increasing adsorption capacity and efficiency.

In contrast, the adsorbent dosage was found to have a negative effect on the adsorption capacity (mg/g). Since capacity is calculated as the amount of Pb(II) adsorbent per unit mass of the material, a lower dosage results in a higher capacity per gram because the available Pb(II) ions are sufficient to saturate the active sites with minimal competition. However, as the adsorbent dosage increases at a fixed Pb(II) concentration, the capacity per gram decreases. This decline is attributed to the split in the concentration gradient across a larger number of particles, which reduces the driving force for adsorption at each individual active site. Additionally, high dosages can trigger particle aggregation or pore blockage, reducing the effective surface area and the availability of active sites (Hashem et al., 2024).

Conversely, the removal efficiency increases with adsorbent weight because more contact surface and active sites become available (Khamseh et al., 2023). Nevertheless, after reaching a certain weight, the increase in efficiency slows down as the system approaches equilibrium between the adsorbed and residual Pb(II) concentrations. Therefore, the adsorbent dosage must be optimized to balance high adsorption capacity (mg/g) with maximum efficiency (%). While low dosage yields high capacity but low removal percentages, excessively high dosage increases efficiency at the cost of capacity and economic efficiency (Majiya et al., 2024).

The contact time factor did not show a significant effect within the tested range (60-120 minutes). This suggests that the adsorption equilibrium was likely reached before the 60-minute mark; thus, extending the contact time further did not significantly improve capacity. While adsorption capacity generally increases with contact time as more ions interact with active sites, this trend only continues until equilibrium is achieved (Hashem et al., 2024). Once the active sites are saturated, additional time provides no further significant enhancement in performance.

Statistical Analysis and Adsorption Behavior.

The statistical analysis based on ANOVA, as shown in **Table 4**, indicates that the developed model is highly significant, with an F-value of 80.62 and a $p\text{-value} < 0.0001$. The lack of fit is not significant ($p > 0.05$), indicating that the model adequately represents the experimental data.

The regression coefficient obtained from the RSM analysis is presented in **Table 5**. The regression coefficient showed that pH had a positive effect on Pb(II) adsorption capacity, while adsorbent dosage exhibited a negative effect. Contact time showed a relatively smaller contribution to the adsorbent response. The VIF values of 1.000 indicated the absence of multicollinearity among the independent variables, confirming that the developed model was statistically reliable and that the variables were independent from one another.

Table 4. ANOVA results for the linear model of Pb(II) adsorption capacity

Source	Sum of Squares	df	Mean Square	F-Value	p-Value	
Model	13948.46	3	4649.49	80.62	< 0.0001	Significant
A - pH	843.64	1	843.64	14.63	0.0015	Significant
B - Contact time	27.19	1	27.19	0.4715	0.5021	Not significant
C -Adsorbent dosage	13077.63	1	13077.63	226.75	< 0.0001	Significant
Residual	922.77	16	57.67			
Lack of Fit	476.99	11	43.36	0.4864	0.8517	Not significant
Pure error	445.78	5	89.16			
Cor Total	14871.23	19				

R^2 = 0.9379; Adjusted R^2 = 0.9263; Predicted R^2 = 0.9131; Adequate Precision = 27.676

Table 5. Regression coefficients of the coded factors for Pb(II) adsorption capacity

Factor	Coefficient estimate	df	Standard error	95% CI Low	95% CI High	VIF
Intercept	65.64	1	1.70	62.04	69.24	
A - pH	9.19	1	2.40	4.09	14.28	1.0000
B - Contact time	1.65	1	2.40	-3.44	6.74	1.0000
C – Adsorbent dosage	-36.16	1	2.40	-41.25	-31.07	1.0000

The relationship between the independent variables and Pb(II) adsorption capacity was represented using a polynomial equation generated by RSM analysis. The coded equation obtained for Pb(II) adsorption capacity is expressed as follows:

$$Y = 65.64 + 9.19A + 1.65B - 36.16C \tag{9}$$

where Y is the adsorption capacity (mg/g), A represents pH, B represents contact time, and C represents adsorbent dosage.

The coefficient estimates indicate that pH had a positive effect on adsorption capacity (coefficient = +9.19), indicating that higher pH enhances Pb(II) adsorption due to reduced competition between H^+ ions and Pb^{2+} ions and increased availability of active sites on the magMCM-41 surface. Meanwhile, adsorbent dosage exerted a negative effect (coefficient = -36.16), confirming that increasing adsorbent mass at a fixed Pb(II) concentration reduces the adsorption capacity per unit mass due to the distribution of available Pb^{2+} ions across a greater number of active sites and possible aggregation of adsorbent particles.

Contact time showed a positive but not significant coefficient (+1.65), suggesting that the adsorption equilibrium was reached within the shortest tested contact time of 60 minutes. This behavior was likely associated with the high specific surface area of magMCM-41 (476.744 m^2/g) and its well-ordered mesopore structure, which facilitated rapid diffusion and interaction of Pb^{2+} ions with the active adsorption sites. Similar adsorption behavior has been reported for mesoporous silica-based adsorbents with highly accessible pore channels and large surface areas.

Furthermore, the high values of R^2 (0.9379), adjusted R^2 (0.9263), and predicted R^2 (0.9131) demonstrate excellent agreement between the experimental and predicted data, indicating that the developed model possessed good reliability and predictive capability for describing Pb(II) adsorption onto magMCM-41.

The contour plots illustrated in **Figure 4** demonstrate that increasing the pH from 3 to 5 consistently enhances both the adsorption capacity and efficiency of the magMCM-41 composite. The capacity contours display nearly parallel lines, indicating a relatively weak interaction between pH and contact time. In contrast, the efficiency contours are slightly curved, suggesting a more significant interaction between factor A (pH) and factor B (contact time). While extending the contact time from 60 to 120 minutes resulted in a moderate increase in both responses, the effect was considerably less pronounced than the impact of pH.

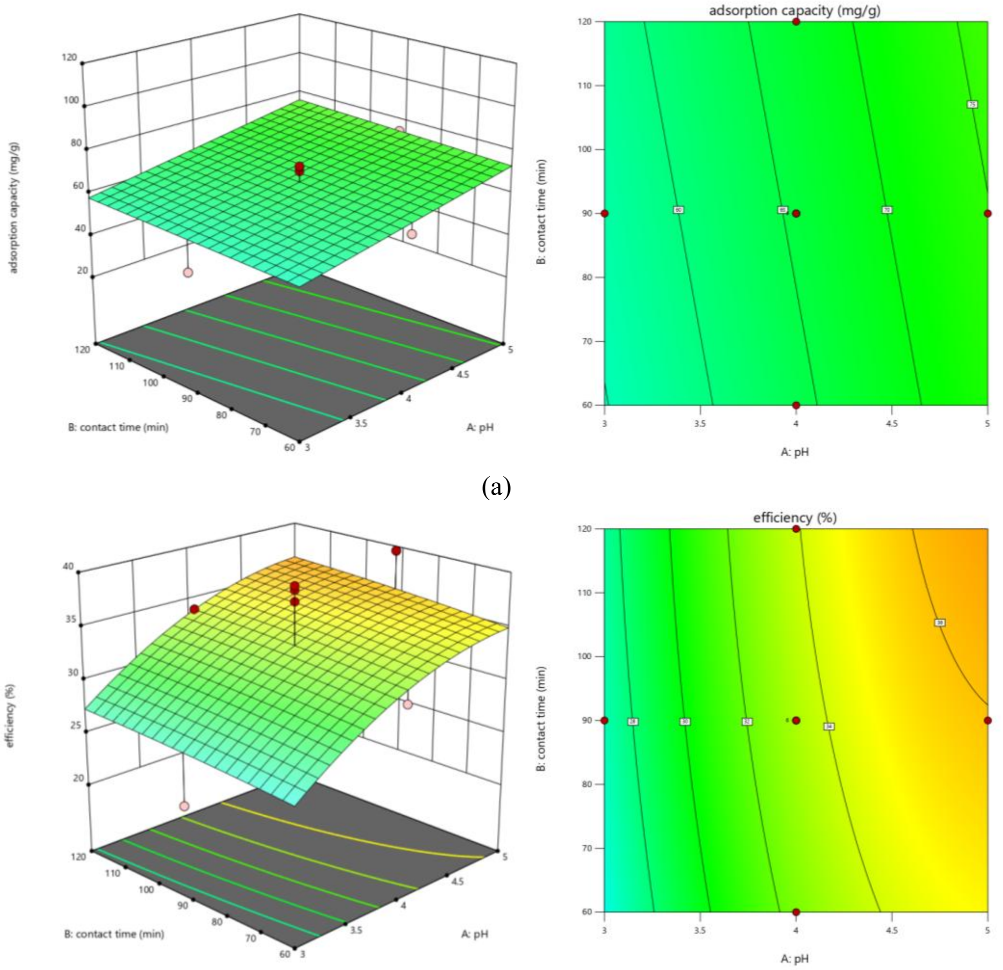

(a)

(b)

Figure 4. Contour plots and 3D response surface plots of adsorption capacity (mg/g) (a) and adsorption efficiency (%) (b) as a function of pH and contact time

Adsorption Isotherm Analysis.

The adsorption equilibrium of Pb(II) onto magMCM-41 was evaluated using Langmuir, Freundlich, Temkin, and Dubinin-Radushkevich (D-R) isotherm models. The fitting parameters are presented in **Table 6,** and the corresponding plots are shown in **Figure 5**. Based on the correlation coefficient (R^2), the D-R model exhibited the best fit (R^2=0.935), indicating that the adsorption process is more suitably described by a pore-filling mechanism on a heterogeneous surface rather than ideal monolayer adsorption (Bbumba et al., 2024). The Langmuir model yielded negative values for both K_L and q_{max} through linear regression, indicating that this model is not applicable to the present system and that the adsorption does not conform to the ideal monolayer assumption on a homogeneous surface.

Table 6. Adsorption isotherm model parameters for Pb

Isotherm Model	Parameter	Value
Langmuir	K_L	-0.0075
	q_{max}	-8.547
	R^2	0.8947
Freundlich	K_F	0.0248
	N	0.6465
	R^2	0.8972

Isotherm Model	Parameter	Value
Temkin	K_T	0.0393
	B_T	59.29
	R^2	0.9085
Dubinin-Radushkevich	K_{DR}	0.0003
	q_{max}	71.3145
	R^2	0.935

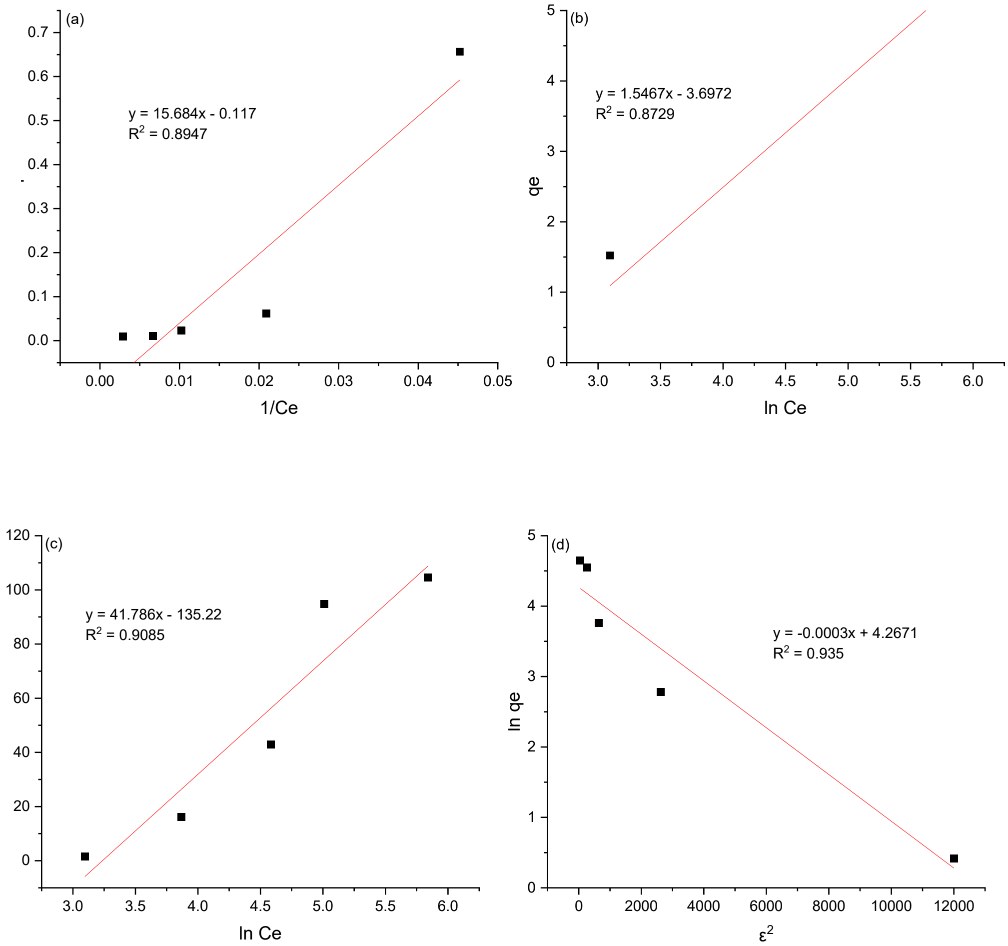

Figure 5. Isotherm model Langmuir (a), Freundlich (b), Temkin (c), and Dubinin-Radushkevich (d)

The Freundlich model showed a moderately high R^2 of 0.8972 with a heterogeneity factor (1/n) of 0.6465 (<1), confirming the magMCM-41 composites that combine amorphous silica and dispersed magnetite phases (Musah et al., 2022). The mean adsorption energy (E) calculated from the D-R model was less than 8 kJ/mol, confirming that the adsorption of Pb(II) onto magMCM-41 is predominantly governed by a physical adsorption (physisorption) mechanism, involving weak interactions such as van der Waals forces and electrostatic attraction between Pb(II) cations and the negatively charged surface functional groups ($Si\text{-}O^-$ and $Fe\text{-}O^-$) at pH 5.

A comparison of the maximum adsorption capacity of magMCM-41 from this study (115.77 mg/g) with previously reported adsorbents for Pb(II) removal is presented in **Table 7**. The capacity achieved in this study is substantially higher than that of unmodified or amino-acid-modified rice husk silica materials, including L-histidine-modified silica (62.5 mg/g, Nurhajawarsi et al., 2018) and L-lysine-modified silica (71.88 mg/g, Rohaeti et al., 2020), demonstrating the advantage of developing an ordered mesoporous structure over conventional silica modification. The capacity of 115.77 mg/g is also competitive with other magnetic mesoporous silica adsorbents reported in the literature, such as Fe_3O_4/MCM-41 composites synthesized from commercial silica sources, which typically report capacities in the range of 80-150 mg/g for Pb(II). Although significantly lower than the amine-functionalized magMCM-41 reported by Kamari et al. (2019) (540.64 mg/g), the difference is expected, given that the amino group ($-NH_2$) grafted on the surface provides strong chemical chelation with Pb(II), whereas the present material relies on physisorption through surface silanol and iron-hydroxyl groups without additional functionalization. The present study, therefore, demonstrates that even without chemical functionalization, the high surface area (476,744 m^2/g) and mesoporous structure of rice husk-derived magMCM-41 alone are sufficient to achieve a competitive adsorption capacity, while maintaining the simplicity and cost-effectiveness of the synthesis process.

Table 6. Adsorption isotherm model parameters for Pb

Isotherm Model	Parameter	Value
Langmuir	K_L	-0.0075
	q_{max}	-8.547
	R^2	0.8947
Freundlich	K_F	0.0248
	N	0.6465
	R^2	0.8972
Temkin	K_T	0.0393
	B_T	59.29
	R^2	0.9085
Dubinin-Radushkevich	K_{DR}	0.0003
	q_{max}	71.3145
	R^2	0.935

Table 7. Comparison of the maximum adsorption capacity of various adsorbents for Pb(II) removal

Adsorbent	q_{max} (mg/g)	Reference
L-histidine-modified silica (rice husk)	62.5	Nurhajawarsi et al. (2018)
L-lysine-modified silica (rice husk)	71.88	Rohaeti et al., (2020)
magMCM-41 (rice husk)	115.77	This study
NH_2-magMCM-41 (rice husk)	540.64	Kamari et al., (2019)

Thermodynamic Study.

The thermodynamic parameters, including Gibbs free energy change (ΔG), enthalpy change (ΔH), and entropy change (ΔS), were calculated and are summarized in **Table 8**.

The negative values ΔG at all temperatures indicate that the adsorption process is spontaneous (Hasani et al., 2022). Additionally, the decrease in ΔG with increasing temperatures suggests that higher temperatures favor the adsorption process.

Table 8. Thermodynamic parameters of Pb(II) adsorption

$-\Delta H°$, J mol^{-1}	$\Delta S°$, J mol^{-1} K^{-1}	$-\Delta G°$, kJ mol^{-1}				R^2
		298	308	318	328	
-22626.5510	-27.9550	-14.2960	8.5822	8.8754	9.1778	0.9572

The negative value of ΔH confirms that the adsorption of Pb(II) onto magMCM-41 is an exothermic process, which is commonly observed in physisorption systems. Meanwhile, the negative value of ΔS indicates a decrease in randomness at the solid-solution interface during adsorption (Raji et al., 2015), suggesting that Pb(II) ions become more ordered when adsorbed onto the surface of magMCM-41.

These findings align with the isotherm analysis, confirming that the adsorption process is dominated by physical interactions and is energetically favorable under the conditions studied.

Conclusion

This study successfully achieved its objectives of synthesizing, characterizing, and evaluating the adsorption performance of magMCM-41 composites derived from rice husk silica and Fe_3O_4 nanoparticles as a low-cost, sustainable adsorbent for Pb(II) removal. Characterization by FTIR, XRD, BET, and PSA confirmed the successful formation of the composite, evidenced by the preservation of both silanol functional groups and the magnetite phase, a high specific surface area of 476.744 m^2/g, a mesoporous pore diameter of 3.83 nm, and an average particle size of 362.7 nm, all of which collectively contribute to its superior adsorption capability and practical magnetic separability. RSM-FCCCD optimization revealed that pH was the dominant positive factor and adsorbent dosage had a negative effect on adsorption capacity, with the maximum capacity of 115.77 mg/g achieved at pH 5 and 0.05 g of adsorbent. Adsorption equilibrium was best described by the Dubinin-Radushkevich isotherm model (R^2=0.935), indicating a physisorption mechanism on a heterogeneous surface, while thermodynamic parameters confirmed that the process was spontaneous and exothermic at all studied temperatures. These results collectively demonstrate that rice husk, an abundant agricultural waste, can be successfully valorized into a high-performance, magnetically recoverable mesoporous adsorbent, offering a practical and sustainable alternative for Pb(II) remediation in aqueous systems.

Reference

Bbumba, S., Karume, I., Nsamba, H. K., Kigozi, M., & Kato, M. (2024). An insight into isotherm models in physical characterization of adsorption studies. *European Journal of Applied Sciences*, *12*(2), 115–134. https://doi.org/10.14738/aivp.122.16738

Chun, J., Mo Gu, Y., Hwang, J., Oh, K. K., & Lee, J. H. (2020). Synthesis of ordered mesoporous silica with various pore structures using high-purity silica extracted from rice husk. *Journal of Industrial and Engineering Chemistry*, *81*, 135–143. https://doi.org/10.1016/j.jiec.2019.08.064

Gabriel, V., Medrano, B., Celis, V. N., & Giraldo, R. I. (2023). Systematic analysis of the nitrogen adsorption-desorption isotherms recorded for a series of microporous – mesoporous amorphous aluminosilicates using classical methods. *Journal of Chemical & Engineering Data*, *68*(9), 2512–2528. https://doi.org/10.1021/acs.jced.3c00257

Ghiasi, A., & Malekpour, A. (2020). Octyl coated cobalt-ferrite/silica core-shell nanoparticles for ultrasonic assisted-magnetic solid-phase extraction and speciation of trace amount of chromium in water samples. *Microchemical Journal*, *154*. https://doi.org/10.1016/j.microc.2019.104530

Hasani, N., Selimi, T., Mele, A., Thaçi, V., Halili, J., Berisha, A., & Sadiku, M. (2022). Theoretical, equilibrium, kinetics and thermodynamic investigations of methylene blue adsorption onto lignite coal. *Molecules*, *27*(6), 1–19. https://doi.org/10.3390/molecules27061856

Hashem, A., Aniagor, C. O., Farag, S., Fikry, M., Aly, A. A., & Amr, A. (2024). Evaluation of the adsorption capacity of surfactant-modified biomass in an aqueous acid blue 193 system. *Waste Management Bulletin*, *2*(1), 172–183. https://doi.org/10.1016/j.wmb.2024.01.004

Hasri, Putri, S. E., Anwar, M., & Askar, M. (2023). Synthesis of rice husk nanosilica using the hydrothermal method. *IOP Conference Series: Earth and Environmental Science*, *1209*(1). https://doi.org/10.1088/1755-1315/1209/1/012011

He, Y., Wu, P., Xiao, W., Li, G., Yi, J., He, Y., Chen, C., Id, P. D., & Duan, Y. (2019). Efficient removal of Pb (II) from aqueous solution by a novel ion imprinted magnetic biosorbent : adsorption kinetics and mechanisms. *PLoS ONE*, *14*(3), 1–17. https://doi.org/10.1371/journal.pone.0213377

Jacobson, A. T., Chen, C., Dewey, J. C., Copeland, G. C., Allen, W. T., Richards, B., Kaszuba, J. P., Duin, A. C. T. Van, Cho, H., Deo, M., She, Y., & Martin, T. P. (2022). Effect of nanoconfinement and pore geometry on point of zero charge in synthesized mesoporous siliceous materials. *JCIS Open*, *8*(November), 100069. https://doi.org/10.1016/j.jciso.2022.100069

Kamari, S., & Ghorbani, F. (2017). Synthesis of magMCM-41 with rice husk silica as cadmium sorbent from aqueous solutions : parameters optimization by response surface methodology. *Environmental Technology*, *38*(12), 1562–1579. https://doi.org/10.1080/09593330.2016.1237557

Kamari, S., & Ghorbani, F. (2021). Extraction of highly pure silica from rice husk as an agricultural by-product and its application in the production of magnetic mesoporous silica MCM–41. *Biomass Conversion and Biorefinery*, *11*(6), 3001–3009. https://doi.org/10.1007/s13399-020-00637-w

Kamari, S., Ghorbani, F., & Sanati, A. M. (2019). Adsorptive removal of lead from aqueous solutions by amine–functionalized magMCM-41 as a low–cost nanocomposite prepared from rice husk: Modeling and optimization by response surface methodology. *Sustainable Chemistry and Pharmacy*, *13*. https://doi.org/10.1016/j.scp.2019.100153

Khamseh, A. A. G., Ghorbanian, S. A., Amini, Y., & Shadman, M. M. (2023). Investigation of kinetic, isotherm and adsorption efficacy of thorium by orange peel immobilized on calcium alginate. *Scientific Reports*, *13*(1), 1–12. https://doi.org/10.1038/s41598-023-35629-z

Kobylinska, N., Kostenko, L., Khainakov, S., & Garcia-Granda, S. (2020). Advanced core-shell EDTA-functionalized magnetite nanoparticles for rapid and efficient magnetic solid phase extraction of heavy metals from water samples prior to the multi-element determination by ICP-OES. *Microchimica Acta*, *187*(5). https://doi.org/10.1007/s00604-020-04231-9

Leong, S. S., Ng, W. M., Lim, J. K., & Yeap, S. P. (2018). Dynamic light scattering: fffective sizing technique for characterization of magnetic nanoparticles. In *Handbook of Materials Characterization*. https://doi.org/10.1007/978-3-319-92955-2

Lu, S., Xu, Q., Liu, M., Zou, D., & Nie, G. (2025). Efficient removal of Pb (II) ions from aqueous solutions using an HFO-PVDF composite adsorption membrane. *Membranes*, *15*(264), 1–17. https://doi.org/10.3390/membranes15090264

Majiya, H., Clegg, F., & Sammon, C. (2024). A chemometric approach using I-optimal design for optimising Pb (II) removal using bentonite-chitosan composites and beads. *Journal of Environmental Management*, *370*, 1–14. https://doi.org/10.1016/j.jenvman.2024.122557

Musah, M., Azeh, Y., Mathew, J. T., Umar, M. T., Abdulhamid, Z., & Muhammad, A. I. (2022). Adsorption kinetics and isotherm models : a review. *Caliphate Journal of Science & Technology (CaJoST)*, *3121*(1), 20–26. https://doi.org/10.4314/cajost.v4i1.3

Nurhajawarsi, N., Rafi, M., Syafitri, U. D., & Rohaeti, E. (2018). L-Histidine-Modified silica from rice husk and optimization of adsorption condition for extractive concentration of Pb(II). *The Journal of Pure and Applied Chemistry Research*, *7*(2), 198–208. https://doi.org/10.21776/ub.jpacr.2018.007.02.402

Rahimah, Fadli, A., Yelmida, Nurfajriani, & Zakwan. (2019). Synthesis and characterization nanomagnetite by co-precipitation. *Indonesian Journal of Chemical Science and Technology*, *02*(02), 90–96. https://doi.org/10.24114/ijcst.v2i2.13995

Raji, F., Saraeian, A., Pakizeh, M., & Attarzadeh, F. (2015). Mesoporous silica MCM-41 modified by ZnCl2: kinetics, thermodynamics, and isotherms. *RSC Advances*, *5*, 37066–37077. https://doi.org/10.1039/C5RA01192B

Rohaeti, E., Primadiska, N. R., & Rafi, M. (2020). Silica modified L-lysine as Pb (II) adsorbent. *AIP Conference Proceedings*, *2243*, 1–9. https://doi.org/10.1063/5.0004766

Soltani, N., Bahrami, A., Pech-Canul, M. I., & González, L. A. (2015). Review on the physicochemical treatments of rice husk for production of advanced materials. In *Chemical Engineering Journal* (Vol. 264, pp. 899–935). Elsevier. https://doi.org/10.1016/j.cej.2014.11.056

Stocki, J., Ku´smierz, M., Sofi ´nska-Chmiel, W., Stankeviˇ, M., Puchala, M., Kojdecki, M. A., Robert, G., & Grajek, H. (2024). Parametric modelling of the crystalline microstructure of the MCM41-type mesoporous silica modified with derivatives of alkyls. *Materials*, *17*(3065), 1–27. https://doi.org/10.3390/ma17133065

Sulejmanović, J., Šabanović, E., Begić, S., & Memić, M. (2019). Molybdenum(VI) oxide-modified silica gel as a novel sorbent for the simultaneous solid-phase extraction of eight metals with determination by flame atomic absorption spectrometry. *Analytical Letters*, *52*(4), 588–601. https://doi.org/10.1080/00032719.2018.1481418

Wu, Q., Xian, Y., He, Z., Zhang, Q., Wu, J., Yang, G., & Zhang, X. (2019). Adsorption characteristics of Pb (II) using biochar derived from spent mushroom substrate. *Scientific Reports*, *9*(15999). https://doi.org/10.1038/s41598-019-52554-2

Wulandari, M., Nofrizal, N., & Sulaiman, S. A. . (2023). A novel approach of using bamboo root cellulose: an alternative for iron(ii) removal from wastewater. *Rasayan Journal of Chemistry*, *16*(2), 921–929. http://doi.org/10.31788/RJC.2023.1628307

Wulandari, M., Syamsudin, N., Azhar, S., & Sulaiman, S. (2022). Tea waste products : a new low-cost and green adsorbent alternative for rhodamine-b dye removal. *Indones. J. Chem*, *22*(6), 1612–1625. https://doi.org/10.22146/ijc.75739

Xu, J., Wang, X., Kang, W., & Zhang, W. (2025). Study on the adsorption of Pb2+ in aqueous solution by alkali modified wheat bran. *Scientific Reports*, *15*(1), 1–12. https://doi.org/10.1038/s41598-025-03876-x